

# Covalently-Bonded Single-Site Ru-N<sub>2</sub> Knitted into Covalent Triazine Frameworks for Boosting Photocatalytic CO<sub>2</sub> Reduction

**Lu Wang**

China University of Petroleum (East China)

**Lin Wang**

China University of Petroleum (East China)

**Saifei Yuan**

China University of Petroleum (East China)

**Liping Song**

China University of Petroleum (East China)

**Hao Ren**

China University of Petroleum (East China) <https://orcid.org/0000-0001-9206-7760>

**Yuankang Xu**

China University of Petroleum (East China)

**Manman He**

China University of Petroleum (East China)

**Yuheng Zhang**

China University of Petroleum (East China)

**Hang Wang**

China University of Petroleum (East China)

**Yichao Huang**

China University of Petroleum (East China)

**Tong Wei**

China University of Petroleum (East China)

**Jiangwei Zhang**

Inner Mongolia University <https://orcid.org/0000-0002-1221-3033>

**Zhuangjun Fan** (✉ [fanzhj666@163.com](mailto:fanzhj666@163.com))

China University of Petroleum (East China)

**Yuichiro Himeda**

National Institute of Advanced Industrial Science and Technology <https://orcid.org/0000-0002-9869-5554>

**Keywords:**

**Posted Date:** April 15th, 2022

**DOI:** <https://doi.org/10.21203/rs.3.rs-1509937/v1>

**License:**  This work is licensed under a Creative Commons Attribution 4.0 International License.

[Read Full License](#)

---

# 1 Covalently-Bonded Single-Site Ru-N<sub>2</sub> Knitted into Covalent Triazine 2 Frameworks for Boosting Photocatalytic CO<sub>2</sub> Reduction

3 Lu Wang,<sup>1</sup> Lin Wang,<sup>\*,1</sup> Saifei Yuan,<sup>1</sup> Liping Song,<sup>1</sup> Hao Ren,<sup>1</sup> Yuankang Xu,<sup>1</sup> Manman He,<sup>1</sup>  
4 Yuheng Zhang,<sup>1</sup> Hang Wang,<sup>1</sup> Yichao Huang,<sup>1</sup> Tong Wei,<sup>1</sup> Jiangwei Zhang,<sup>\*,2</sup> Zhuangjun Fan,<sup>\*,1</sup>  
5 and Yuichiro Himeda<sup>3</sup>

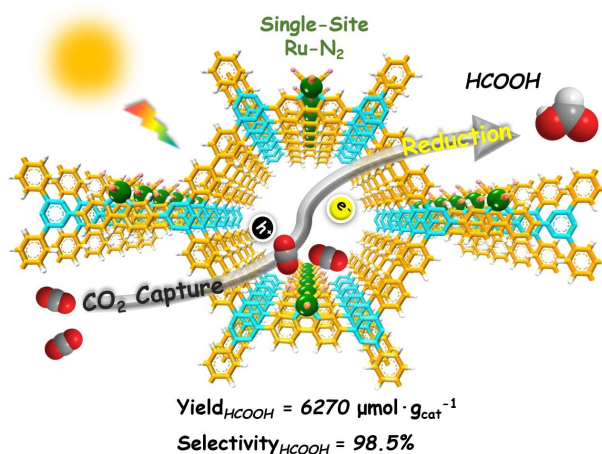
6 <sup>1</sup> School of Materials Science and Engineering, China University of Petroleum (East China),  
7 Qingdao 266580, China

8 <sup>2</sup> Dalian National Laboratory for Clean Energy & State Key Laboratory of Catalysis, Dalian  
9 Institute of Chemical Physics, Chinese Academy of Sciences (CAS), Dalian 116023, China

10 <sup>3</sup> Global Zero Emission Research Center, National Institute of Advanced Industrial Science and  
11 Technology, Tsukuba, Ibaraki 305-8569, Japan

## 12 13 Abstract

14 Developing highly efficient photocatalysts for converting CO<sub>2</sub> into solar fuels is of great  
15 importance for energy sustainability. However, efficient photoreduction of CO<sub>2</sub> over the  
16 heterogeneous catalyst is hindered by lack of precisely controlled active sites and poor contact  
17 between active sites and the semiconductor, which leads to low selectivity and poor photochemical  
18 stability of the catalyst. Herein, utilizing highly stable and readily tunable photoresponsive covalent  
19 triazine frameworks (CTFs) as intriguing platforms, the well-defined molecular catalysts are  
20 directly knitting into CTFs by an *in-situ* covalent-bonding strategy for the first time to afford photo-  
21 responsive single-site Ru CTFs. The robust chemical knitting of molecular catalyst with porous  
22 CTFs provides the atomically dispersed catalytic sites, providing enhanced light absorption and CO<sub>2</sub>  
23 diffusion. Significantly, the resulting Ru-CTF can reduce CO<sub>2</sub> to formic acid under visible light with  
24 excellent selectivity (98.5%) and activity (6270 μmol·g<sub>cat</sub><sup>-1</sup>), which greatly outperforms most other  
25 polymer semiconductors reported so far. However, the homogeneous Ru counterpart  
26 (Ru(dcbpy)(CO)<sub>2</sub>Cl<sub>2</sub>, dcbpy=2,2'-bipyridine-5,5'-dicarbonitrile) exhibits a low activity and  
27 deactivates within 1 h. Systematic investigations reveal that the introduction of single sites (Ru-N<sub>2</sub>)  
28 can promote photoinduced charge separation and CO<sub>2</sub> activation, thus significantly enhancing the  
29 photocatalytic performance. The combination of *in-situ* fourier transform infrared spectrometer (*in-*  
30 *situ* FTIR), density functional theory (DFT) calculations and luminescence quench experiments  
31 were particularly investigated to confirm the possible photocatalytic CO<sub>2</sub> reduction mechanism over  
32 Ru-CTF. This work provides a new pathway and significant insights into the design of CTF-based  
33 single-site photocatalysts for highly selective CO<sub>2</sub> photoreduction.



34

35

### Graphical Abstract

## 36 Introduction

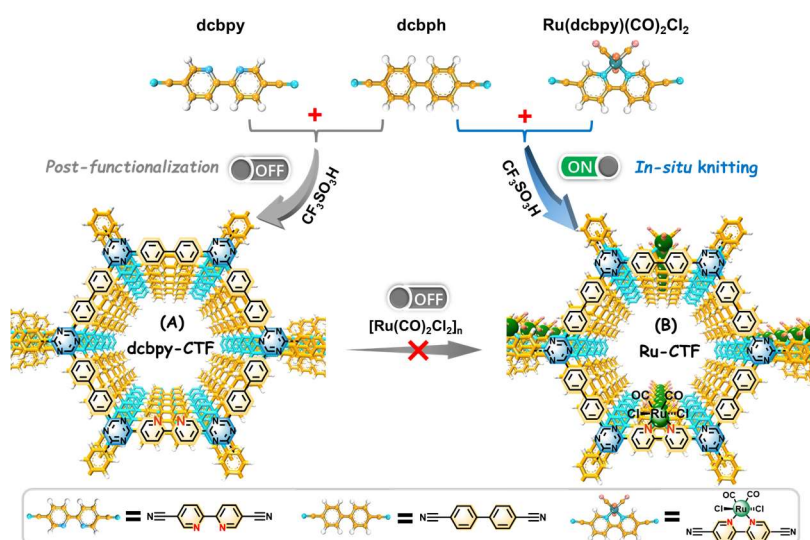
37 The solar-light-driven CO<sub>2</sub> reduction reaction (CO<sub>2</sub>RR) is expected to perfectly mimic natural  
 38 photosynthesis and enables the sustainable production of solar fuels or high-value-added chemicals  
 39 in a more environmentally friendly manner.<sup>1</sup> Among the CO<sub>2</sub> conversion strategies, the selective  
 40 reduction of CO<sub>2</sub> to liquid formic acid (HCOOH) via photocatalysis possesses broad application  
 41 prospects.<sup>2,3</sup> It is a promising liquid organic hydrogen carrier that can store and release H<sub>2</sub> in the  
 42 presence of a suitable catalyst.<sup>4,5</sup> The reduction/re-oxidation process thus can complete a carbon-  
 43 neutral cycle without release of harmful byproducts.<sup>6</sup> This strategy can create renewable energy  
 44 fuels and chemical raw materials, which has important scientific research value in the field of energy  
 45 storage and transformation.

46 To attain high CO<sub>2</sub>RR activity and selectivity, various semiconductor catalysts, such as Ta<sub>2</sub>O<sub>5</sub>,<sup>7</sup>  
 47 TiO<sub>2</sub>,<sup>8</sup> and *g*-C<sub>3</sub>N<sub>4</sub>,<sup>9,10</sup> have been implemented. However, these traditional semiconductor-based  
 48 photocatalysts are usually difficult to atomic-scale regulate and control the photoelectrochemical  
 49 performances, hampering the improvements on the photocatalytic performance. Since pioneered by  
 50 Thomas,<sup>11</sup> porous covalent triazine frameworks (CTFs) have emerged as a new type of porous  
 51 materials showing a variety of promising applications including in CO<sub>2</sub> capture and storage,  
 52 photocatalysis and energy storage due to their  $\pi$ -conjugated nitrogen-rich structures, large surface  
 53 areas, and very high thermal, chemical and mechanical stabilities.<sup>12-15</sup> Compared to the traditional  
 54 trimerization process catalyzed by Lewis acids such as ZnCl<sub>2</sub> at elevated temperatures (400°C), the  
 55 catalytic process by using trifluoromethanesulfonic acid (CF<sub>3</sub>SO<sub>3</sub>H) as the catalyst affords high-  
 56 quality CTFs with minimized surface carbonization as efficient photocatalysts.<sup>16-18</sup> CTFs as the  
 57 versatile platforms can effectively integrate a molecular catalyst via selection of appropriate  
 58 bridging ligands with triazine units as connecting nodes, thereby enabling efficient  
 59 photosensitization of multielectron reduction catalysis.<sup>16</sup> For example, the ligand of 2,2'-bipyridine-

60 5,5'-dicarbonitrile (dc bpy) is an ideal linker for constructing functionalized CTFs photocatalysts for  
61 photocatalytic CO<sub>2</sub> reduction due to the strong coordination ability of its bipyridine unit.<sup>19,20</sup>

62 In recent years, several ruthenium(II)-based photocatalytic molecular catalysts have been  
63 employed as high-selective active sites to produce HCOOH under visible light.<sup>6,9,21-22</sup> However, it  
64 is difficult for homogeneous molecular catalytic systems to isolate the products and recycle the  
65 catalysts.<sup>23,24</sup> Promisingly, molecular active sites anchored on porous materials as heterogeneous  
66 catalysts can prevent the dimerization of the molecular catalyst and its deactivation, which are  
67 expected to achieve better photocatalytic performance and recyclability.<sup>18,25-26</sup> The knitting of a  
68 molecular catalyst into the photo-responsive porous materials can not only enhance the  
69 photocatalytic performances by stabilizing the molecular catalyst and promoting electron transfer  
70 between frameworks and active catalysts,<sup>26</sup> but also facilitate the photocatalysis without any  
71 additional costly photosensitizers.<sup>27</sup> This synthetic tunability in conjunction with the improved  
72 durability of the molecular catalytic units grants the catalyst-modified frameworks benefits of both  
73 homogeneous and heterogeneous catalysts.<sup>19</sup> At present, the development of photocatalytic CO<sub>2</sub>  
74 reduction to HCOOH with high selectivity and high activity based on stable CTFs has encountered  
75 a bottleneck due to the lack of precise and controllable catalytic centers on the stable supports. It is  
76 necessary to develop a method to integrate light harvesters and highly active and selective catalytic  
77 sites on CTF structures for photocatalytic CO<sub>2</sub> reduction to produce formic acid.

78 Herein, we report a newly devised photocatalyst via a new strategy for the first time by knitting  
79 the precise single-atom site (Ru(dc bpy)(CO)<sub>2</sub>Cl<sub>2</sub>) into the photo-responsive CTFs for highly  
80 selective photoreduction of CO<sub>2</sub> to HCOOH. Firstly, the strategy of post-modification of Ru metal  
81 sites into a preformed framework (dc bpy-CTF, Fig. 1A) was unsuccessful due to the preformed  
82 frame dc bpy-CTF cannot be synthesized by the superacid method, resulting from the formation of  
83 a salt by the reaction of pyridine moieties with trifluoromethanesulfonic acid (Fig. 1 and  
84 Supplementary Fig. 5).<sup>28</sup> Significantly, employing metal-coordinating molecules as building blocks  
85 was successfully applied to *in-situ* construct the single-site photocatalysts (Ru-CTFs, Fig. 1B).  
86 Therefore, the molecular catalysts direct knitted CTFs with robust covalently-bonded interfacial  
87 contact and high charge transfer efficiency can be constructed, which would benefit the spatial  
88 separation of photogenerated carriers. In addition, this effectively knitted strategy can prevent the  
89 dimerization of the molecular active sites and its deactivation, thus leading to better photocatalytic  
90 performance and recyclability.



91

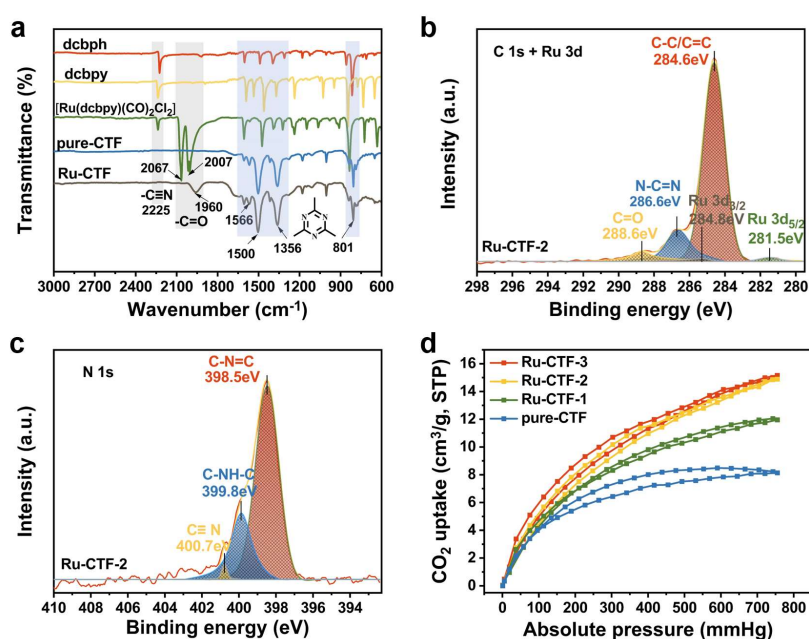
92 **Fig. 1 Schematic representation of the *in-situ* knitting strategy for Ru-CTFs.**

### 93 **Results**

94 **Synthesis and characterization.** According to the synthetic approach in Fig. 1, four Ru-CTFs with  
 95 different molar amounts of  $\text{Ru(dcbpy)(CO)}_2\text{Cl}_2$  ( $X=0, 0.01, 0.025, 0.1$ ) and dcbph precursor ( $0.6-$   
 96  $X$ ) were fabricated and named as pure-CTF, Ru-CTF-1, Ru-CTF-2, and Ru-CTF-3, respectively (see  
 97 the details in Supplementary Fig. 4). The structures of the synthesized CTFs were first confirmed  
 98 by using the Fourier transform infrared (FT-IR) technique (as shown in Fig. 2a). The successful  
 99 formation of triazine structures in these CTFs were confirmed by the C=N stretching bands ( $1566,$   
 100  $1500$  and  $801\text{ cm}^{-1}$ ) and C-N stretching vibration band ( $1356\text{ cm}^{-1}$ ) in the FT-IR spectra. Additionally,  
 101 the absence of a vibrational band for the terminal cyano group at  $2225\text{ cm}^{-1}$  indicating the high  
 102 degree of polymerization.<sup>17,29-31</sup> Compared to the spectrum of pure-CTF, an additional peak at  $1960$   
 103  $\text{cm}^{-1}$  was observed in the spectrum of Ru-CTF, which were attributed to the stretching vibration of  
 104  $\nu(\text{C}=\text{O})$  in the  $\text{Ru(dcbpy)(CO)}_2\text{Cl}_2$  moiety, thus indicating the molecular active sites were  
 105 successfully knitted in the CTFs.<sup>32</sup> Notably, compared with vibration of  $\nu(\text{C}=\text{O})$  in the complex  
 106  $\text{Ru(dcbpy)(CO)}_2\text{Cl}_2$  ( $2072$  and  $2011\text{ cm}^{-1}$ ), Ru-CTF exhibited a red shift in the  $\nu(\text{C}=\text{O})$  stretching  
 107 vibration ( $1960\text{ cm}^{-1}$ ), indicating that CO dissociation occurred in the *in-situ* synthetic process.<sup>8,33</sup>  
 108 X-ray photoelectron spectroscopy (XPS) was further employed to analyze the chemical states and  
 109 structural insight of CTFs. As compared with pure-CTF (Supplementary Fig. 10), the additional  
 110 peaks in the high-resolution C 1s + Ru 3d spectrum of Ru-CTF (Fig. 2b) at about  $281.5\text{ eV}$  and  
 111  $284.8\text{ eV}$  were assigned to  $\text{Ru}^{\text{II}}\ 3d_{5/2}$  and  $3d_{3/2}$  states, respectively.<sup>34</sup> Moreover, these values  
 112 correspond well with previous reports on the hexacoordinated  $[\text{Ru}^{\text{II}}-\text{N}_6]$  system.<sup>35-36</sup> Three similar  
 113 emission features in the high-resolution N 1s spectrum for Ru-CTF (Fig. 2c) were observed at  $398.5$   
 114  $\text{eV}$  (C-N=C),  $400.7\text{ eV}$  (C $\equiv$ N), and  $399.8\text{ eV}$  (C-NH-C), respectively, which were located at higher

115 binding energy as compared to pure-CTF (Supplementary Fig. 10).<sup>37</sup> The observed chemical shifts  
 116 demonstrated the successful synthesis of Ru-knitted CTFs and the influence of Ru doping on the  
 117 electronic properties of the frameworks.<sup>38</sup> Additionally, the successful incorporation of Ru units  
 118 was further supported by the elemental mapping analysis by energy-dispersive X-ray spectroscopy  
 119 (EDX) (Supplementary Fig. 11) and inductively coupled plasma-atomic emission spectrometry  
 120 (ICP-AES). After the introduction of Ru sites, the structures of these Ru-CTFs were maintained as  
 121 confirmed by Raman studies. As shown in Supplementary Fig. 13, the Raman spectra of all Ru-  
 122 CTFs were both similar, indicating a similar structure of these Ru-CTFs to that of pure-CTF. The  
 123 strongest  $G^+$  peak at  $1613\text{ cm}^{-1}$  is an indication of a well-ordered  $sp^2$  planar structure. The G peak  
 124 and D peak at  $1519$  and  $1416\text{ cm}^{-1}$  relate to the distortion and carbon defects in each layer,  
 125 respectively.<sup>39,40,41</sup>

126 In addition, volumetric  $\text{CO}_2$  adsorption measurements (Fig. 2d) revealed the increased uptake  
 127 after knitting of the  $\text{Ru}(\text{dcbpy})(\text{CO})_2\text{Cl}_2$  despite a similar BET surface area (Supplementary Fig. 14).  
 128 The improved  $\text{CO}_2$  adsorption capacity may be attributed to the enhanced interaction between the  
 129  $\text{CO}_2$  molecules and the coordination unsaturated  $\text{Ru}(\text{dcbpy})(\text{CO})_2\text{Cl}_2$  centers.<sup>42,43</sup> The higher  $\text{CO}_2$   
 130 capture capability for Ru-CTFs offers more possibilities for  $\text{CO}_2$  access and transport in the porous  
 131 structure, which is vital for the following  $\text{CO}_2$  conversion at pore surface and active sites.



132

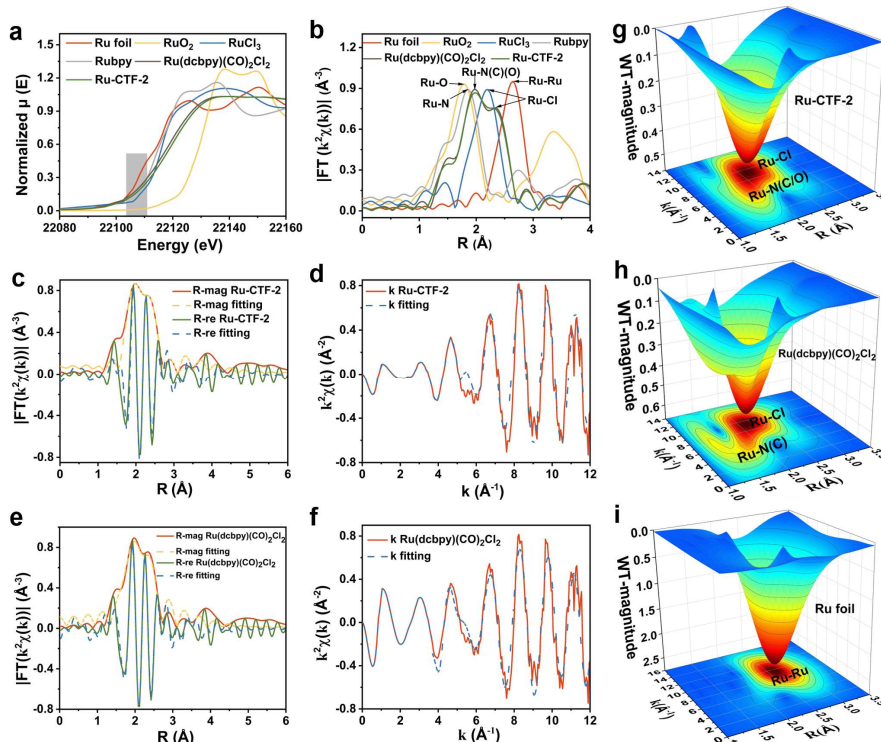
133 **Fig. 2 Characterization of the CTFs.** (a) FT-IR spectra of CTFs and precursor. (b) C 1s +Ru 3d  
 134 and (c) N 1s XPS spectra of Ru-CTF. (d) 273K  $\text{CO}_2$  adsorption-desorption isotherms of CTFs.

135 To further confirm the local coordination environment of single Ru atoms in the Ru-CTF  
 136 catalyst, the X-ray absorption near-edge structure (XANES) spectroscopy and extended X-ray  
 137 absorption fine structure (EXAFS) analyses of the Ru-CTF as well as the reference systems  
 138 ( $\text{Ru}(\text{dcbpy})(\text{CO})_2\text{Cl}_2$ , Ru foil,  $\text{RuO}_2$ ,  $\text{RuCl}_3$ , and Rubpy) were then carried out in detail (Fig. 3). As

139 shown in the Ru K-edge XANES spectra (Fig. 3a), the energy absorption threshold values of Ru-  
140 CTF and Ru(dcbpy)(CO)<sub>2</sub>Cl<sub>2</sub> are higher than that of Ru foil and lower than that of RuCl<sub>3</sub>, and  
141 overlapping the position of tris(2,2'-bipyridyl)dichlororuthenium(II) hexahydrate (Rubpy),  
142 implying that the stable valences state of Ru is +2 in Ru-CTF and Ru(dcbpy)(CO)<sub>2</sub>Cl<sub>2</sub>, which is  
143 consistent with the result of XPS analysis. Expectedly, Ru-CTF gave nearly the same signals as the  
144 Ru(dcbpy)(CO)<sub>2</sub>Cl<sub>2</sub> precursor, which indicates that the valence state of Ru in Ru(dcbpy)(CO)<sub>2</sub>Cl<sub>2</sub>  
145 does not change during the preparation of Ru-CTF framework. In addition, from the k<sup>2</sup>-weighted  
146 Fourier transformed EXAFS (FT-EXAFS) for the Ru K-edge of Ru-CTF and Ru(dcbpy)(CO)<sub>2</sub>Cl<sub>2</sub>  
147 sample (Fig. 3b), the main peak at 1.97 Å was corresponding to the Ru–N(C)(O) coordination  
148 environment. The shoulder peak located at 2.36 Å was attribute to scattering path of Ru–Cl bonds  
149 for Ru-CTF and Ru(dcbpy)(CO)<sub>2</sub>Cl<sub>2</sub>. In contrast to the Ru foil, Ru-CTF did not present a prominent  
150 peak at the positions of Ru–Ru bonds located at 2.64 Å, supporting the conclusion that the atomically  
151 dispersed Ru atom was anchored on the CTF framework. By comparing the scattering path intensity  
152 of Ru–N(C)(O) bonds in Ru-CTF and Ru(dcbpy)(CO)<sub>2</sub>Cl<sub>2</sub>, the Ru–N(C)(O) coordination number  
153 in Ru-CTF was much lower than that in Ru(dcbpy)(CO)<sub>2</sub>Cl<sub>2</sub>, indicating that CO dissociation had  
154 occurred in the synthesis process, which was also consistent with the result of FTIR characterization.  
155 In addition, the wavelet transform EXAFS (WT-EXAFS) can intuitively demonstrate the local  
156 coordination environment of Ru-CTF catalyst (Fig. 3g-i and Supplementary Fig. 16). Compared  
157 with the characteristic scattering path signal of Ru–Ru bond in the Ru foil located at [9.66, 2.83],  
158 no characteristic peak corresponding to Ru–Ru coordination was detected in the Ru-CTF, thus  
159 indicating the successful construction of single-site Ru catalytic center.

160 Moreover, quantitative  $\chi(R)$  and  $\chi(k)$  space spectra fitting were also performed to investigate  
161 local atomic structure and further obtain the coordination numbers of Ru in Ru-CTF and  
162 Ru(dcbpy)(CO)<sub>2</sub>Cl<sub>2</sub>. As depicted in Fig. 3c-f, the EXAFS fitting curve in k space and R space for  
163 Ru-CTF and Ru(dcbpy)(CO)<sub>2</sub>Cl<sub>2</sub> samples suggested that the coordination number of the central  
164 atom Ru is six. In addition, the local structural parameters were provided in Supplementary Table 1.  
165 In Ru K-edge  $\chi(R)$  space spectra, Ru(dcbpy)(CO)<sub>2</sub>Cl<sub>2</sub> displayed Ru-C bonding with coordination  
166 number (CN) approaching 2 [CN=N\*amp=5\*(0.83+/- 0.13)] at 1.93 Å and Ru-N bonding with  
167 coordination number (CN) approaching 2 [CN=N\*amp=2\*(0.85+/- 0.11)] at 2.04 Å, while Ru-Cl  
168 bonding with coordination number (CN) approaching 2 [CN=N\*amp=2\*(0.80+/- 0.16)] at 2.37 Å.  
169 As a contrast, Ru-CTF displayed Ru-N bonding with coordination number (CN) approaching  
170 2[CN=N\*amp=2\*(0.85+/-0.11)] at 2.04 Å, Ru-Cl bonding with coordination number (CN)  
171 approaching 2 [CN=N\*amp=2\*(0.80+/- 0.16)] at 2.37 Å, which were consistent with  $\chi(R)$  space  
172 spectra fitting curve of Ru(dcbpy)(CO)<sub>2</sub>Cl<sub>2</sub>. Significantly, Ru-CTF displayed Ru-C bonding with  
173 coordination number (CN) approaching 1[CN=N\*amp=1\*(0.83+/-0.13)] at 1.93 Å, Ru-O bonding

174 with coordination number (CN) approaching 1 [ $CN=N \cdot \mu = 1 \cdot (0.84 \pm 0.15)$ ] at 2.10 Å, thus  
 175 clearly indicating that one CO detached from Ru atoms in Ru-CTF with extra one H<sub>2</sub>O molecule  
 176 coordination. The good fitting result of  $\chi(R)$  and  $\chi(k)$  space spectra with reasonable R-factor  
 177 quantitatively support the local atomic structure and coordination numbers information discussed in  
 178 Ru-CTF and Ru(dcbpy)(CO)<sub>2</sub>Cl<sub>2</sub> above.



179  
 180 **Fig. 3 X-ray absorption near-edge structure (XANES) spectroscopy and extended X-ray**  
 181 **absorption fine structure (EXAFS) analyses of the Ru-CTF. (a)** Normalized Ru K-edge XANES  
 182 spectra and **(b)** corresponding  $k^2$ -weighted Fourier transform spectra from Ru K-edge EXAFS of  
 183 Ru foil, RuO<sub>2</sub>, RuCl<sub>3</sub>, Rubpy, Ru(dcbpy)(CO)<sub>2</sub>Cl<sub>2</sub> and Ru-CTF.  $\chi(R)$  space spectra fitting curve of  
 184 EXAFS spectra of **(c)** Ru-CTF and **(e)** Ru(dcbpy)(CO)<sub>2</sub>Cl<sub>2</sub>.  $k^2\chi(k)$  space spectra fitting curve of **(d)**  
 185 Ru-CTF and **(f)** Ru(dcbpy)(CO)<sub>2</sub>Cl<sub>2</sub>. 3D contour WT-EXAFS map with 2D projection of **(g)** Ru-  
 186 CTF, **(h)** Ru(dcbpy)(CO)<sub>2</sub>Cl<sub>2</sub>, **(i)** Ru foil.

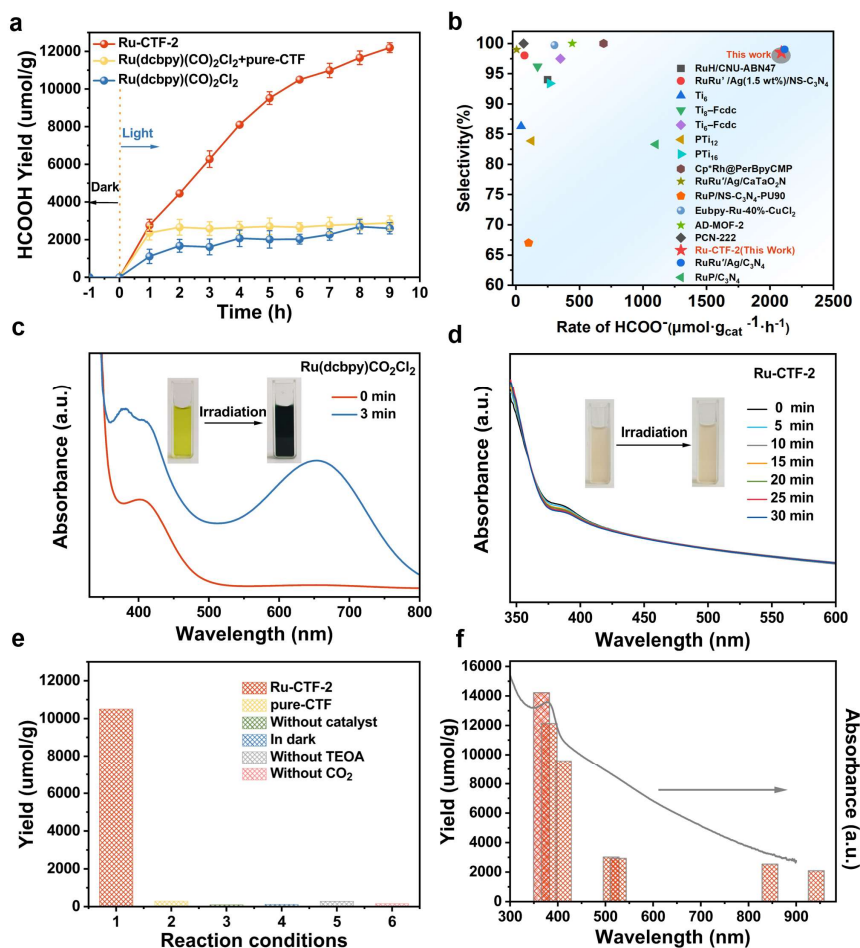
187 **Photocatalytic CO<sub>2</sub> reduction performance.** The photocatalytic CO<sub>2</sub> reduction activity was tested  
 188 under visible light irradiation (Supplementary Fig. 17). It can be seen that the generated formate  
 189 increased with appropriate increase of Ru content in the CTFs (Supplementary Fig. 18), while with  
 190 the increase of more Ru content, the color of the catalyst gradually deepens (Supplementary Fig.  
 191 19), thus causing the weak light transmittance and less efficient light utilization.<sup>44</sup> As shown in Fig.  
 192 4a, under continuous visible light illumination, formate production of Ru-CTF exhibits a time-  
 193 dependent increase. The average formation rate of HCOO<sup>-</sup> is 2090  $\mu\text{mol} \cdot \text{g}_{\text{cat}}^{-1} \cdot \text{h}^{-1}$  in 3 h, which is  
 194 higher than that of most previous catalysts (Fig. 4b and Supplementary Table 4). In contrast, the  
 195 amount of produced HCOO<sup>-</sup> with homogeneous Ru(dcbpy)(CO)<sub>2</sub>Cl<sub>2</sub> and physically mixed

196 Ru(dcbpy)(CO)<sub>2</sub>Cl<sub>2</sub> with pure-CTF (1.34 wt% of Ru(dcbpy)(CO)<sub>2</sub>Cl<sub>2</sub>), respectively, remains almost  
197 unchanged from 1 to 9 hours possibly due to the dimerization-driven deactivation. Rapid  
198 deactivation of the homogeneous system was supported by time-dependent HCOO<sup>-</sup> production and  
199 obvious changes from 600 to 700 nm of Ru(dcbpy)(CO)<sub>2</sub>Cl<sub>2</sub> upon light irradiation in UV-Vis  
200 absorption graph (Fig. 4c). In contrast, the UV-Vis absorption graph of Ru-CTF showed almost no  
201 change with the extension of light irradiation time (Fig. 4d). Additionally, the inset image in Fig. 4d  
202 showed almost no color change after the photocatalytic reaction for heterogeneous Ru-CTF, while  
203 the color of homogeneous Ru(dcbpy)(CO)<sub>2</sub>Cl<sub>2</sub> (inset in Fig. 4c) changed from yellow to dark green  
204 upon light irradiation. Therefore, the above results further show that the anchored molecular active  
205 sites in CTFs as heterogeneous catalysts can prevent the dimerization of the molecular catalyst and  
206 its deactivation, thus resulting in a better photocatalytic performance. As a solid catalyst, Ru-CTF  
207 was recycled and reused at least three runs without a significant decrease in activity (Supplementary  
208 Fig. 20), demonstrating the robust stability with the extended reaction duration, and this slight  
209 decrease may be due to the recovery loss during the reaction process. Besides, from the FTIR, DRS  
210 and Raman analyses of the recovered Ru-CTF, no substantial changes can be observed after three  
211 cycles (Supplementary Fig. 21), confirming the high durability of Ru-CTF. These observations  
212 further illuminate that incorporation of molecular catalysts with porous materials can be an  
213 effectively heterogenized approach for easy product isolation and catalyst recycle, prolonging their  
214 service lives.

215 Control experiments are conducted to further understand the CO<sub>2</sub> reduction under various  
216 conditions (Fig. 4e). First of all, negligible activity in the absence of TEOA under otherwise identical  
217 conditions. Additionally, the CO<sub>2</sub> reduction process was also investigated in the absence of visible  
218 light, and the whole reaction was immediately terminated, verifying that the CO<sub>2</sub> reduction is indeed  
219 driven by the photoirradiation. Furthermore, when N<sub>2</sub> was used as the feedstock gas instead of CO<sub>2</sub>,  
220 bare of HCOO<sup>-</sup> was detected from the catalytic process, suggesting that the generated formate should  
221 originate from the CO<sub>2</sub> reactant. Formate as the liquid product was detected and quantified by the  
222 HPLC technology (Supplementary Fig. 22). In addition, the gaseous products were detected and  
223 quantified by gas chromatography (GC), indicating only traces of gaseous CO and CH<sub>4</sub> were tested  
224 as the byproducts (Supplementary Fig. 24). As a consequence, super high selectivity for CO<sub>2</sub>-to-  
225 HCOOH photosynthesis was obtained by Ru-CTF (98.5 %, Supplementary Fig. 25). In comparison,  
226 the selectivity for CO<sub>2</sub>-to-HCOOH photosynthesis by homogeneous Ru(dcbpy)(CO)<sub>2</sub>Cl<sub>2</sub> (86.1%)  
227 and physically mixed Ru(dcbpy)(CO)<sub>2</sub>Cl<sub>2</sub> with pure-CTF (81.4%) was much lower than that of Ru-  
228 CTF.

229 To further prove that the reaction is driven by light absorption, the activities for HCOO<sup>-</sup>  
230 generation over Ru-CTF were carried out at different wavelengths. The dependence of HCOO<sup>-</sup>

231 production on irradiation wavelength showed that the trend of  $\text{HCOO}^-$  generation matched well  
 232 with the photon absorption characteristics of Ru-CTF (Fig. 4f), confirming that the reaction was  
 233 indeed induced by light excitation of Ru-CTF. Notably,  $\text{HCOO}^-$  can even be produced even at 942  
 234 nm (near-infrared region) as shown in Fig. 4f, indicating the wide light-responsive capacity of Ru-  
 235 CTF.



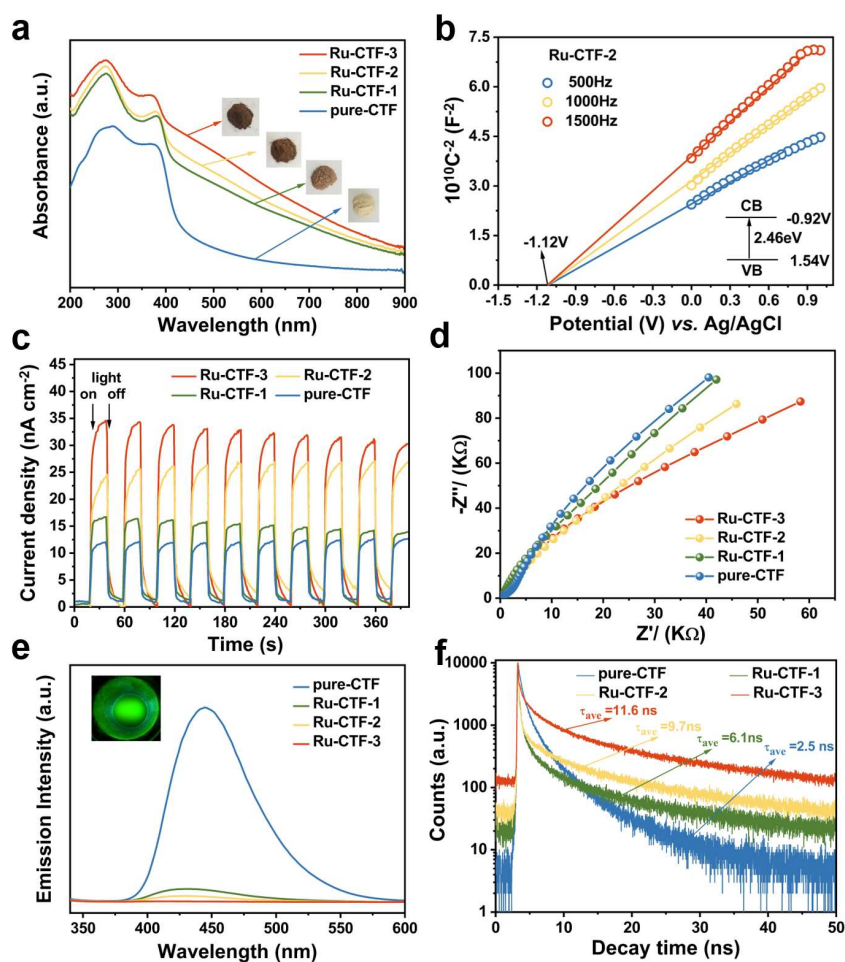
236  
 237 **Fig. 4 Photocatalytic  $\text{CO}_2$  reduction performance.** (a) Amount of  $\text{HCOO}^-$  generated from  $\text{CO}_2$  as  
 238 a function of the irradiation time over heterogeneous Ru-CTF, homogeneous Ru(dcbpy)( $\text{CO}$ ) $_2$ Cl $_2$ ,  
 239 and physically mixed Ru(dcbpy)( $\text{CO}$ ) $_2$ Cl $_2$  with pure-CTF. Reaction conditions:  $\lambda > 400$  nm;  
 240 Photocatalyst: 0.5 mg/ml; DMA/TEOA volume ratio: 3/1. (b) Comparison of  $\text{HCOO}^-$  selectivity  
 241 and activity of reported photocatalysts without extra photosensitizer under visible light irradiation.  
 242 UV-Vis absorption changes for (c) homogeneous Ru(dcbpy)( $\text{CO}$ ) $_2$ Cl $_2$  and (d) heterogeneous Ru-  
 243 CTF in DMA at different irradiation times. (e) Amount of  $\text{HCOO}^-$  generated from  $\text{CO}_2$  in the  
 244 catalytic system under different reaction conditions. (f) Wavelength dependent  $\text{HCOO}^-$  production  
 245 in photocatalytic  $\text{CO}_2$  reduction. (Reaction time is 6h in e, f)

246 **Photoelectrochemical measurements.** In order to understand the excellent photocatalytic activity  
 247 of Ru-CTFs, we further characterized the optical properties and analyzed the electronic structures

248 of the materials. As suggested by the UV-Vis diffuse reflection spectra (DRS) (Fig. 5a), the strong  
249 visible light absorption of pure-CTF only extended to ca. 600 nm, while Ru-CTFs showed a much  
250 broader light absorption range up to 900 nm. The broader light absorption range was ascribed to the  
251 MLCT (metal-to-ligand charge transfer) processes of Ru(dcbpy)(CO)<sub>2</sub>Cl<sub>2</sub> at the absorption from  
252 400 to 500 and 610 to 700 nm (Supplementary Fig. 28), in which the electrons were excited from  
253 an occupied metal-localized orbital to a vacant ligand-localized orbital, thus resulting in the long-  
254 wavelength light absorption.<sup>45,46</sup> Notably, an obvious red-shift of the optical absorption edge  
255 occurred upon increasing the content of Ru units in the structure, plus with a decrease in the optical  
256 band gap from 2.75 to 2.28 eV by their Tauc plots (Supplementary Fig. 29), respectively.<sup>47</sup> In order  
257 to illustrate their semiconductor characters and the possibility for the subsequent CO<sub>2</sub>  
258 photoreduction study, the Mott–Schottky measurements on CTFs were performed at a frequency of  
259 500, 1000, and 1500 Hz. The positive slope of the obtained C<sup>-2</sup> values (vs. the applied potentials)  
260 was consistent with those of typical n-type semiconductors (Fig. 5b and Supplementary Fig. 30).  
261 The bottom of the conduction bands (CB) of CTFs were calculated to be from -0.92 to -0.77 V (the  
262 higher Ru loading, the more negative), respectively, versus the normal hydrogen electrode (NHE),  
263 which were all enough for the conversion of CO<sub>2</sub> to formate (-0.61 V vs. NHE). Therefore, it is  
264 theoretically feasible for the photocatalytic reduction of CO<sub>2</sub> to generate formate by utilizing Ru-  
265 CTFs.

266 The photoresponses of Ru-CTFs and pure-CTF catalysts were characterized by the  
267 chronoamperometric I-t curves under chopped illumination condition. As expected, the Ru-CTFs  
268 catalyst showed higher responses than the pristine pure-CTF, indicating the higher efficiency for the  
269 separation of electron-hole in the Ru-CTFs (Fig. 5c). The fast charge transfer capability is further  
270 confirmed by electrochemical impedance spectroscopy (EIS). As shown in Fig. 5d, the small arc  
271 radius of Nyquist plot of the Ru-CTFs electrode indicated that the photogenerated electron–hole  
272 pairs in Ru-CTFs could be more efficiently separated by the ligand-metal charge transfer effect,<sup>47</sup>  
273 which contributed to the improved photocatalytic activity. The measured steady-state  
274 photoluminescence (PL) spectra as shown in Fig. 5e suggested that the intrinsic emission peaks  
275 greatly decreased in the presence of Ru unit, indicating a relatively low recombination rate of  
276 electrons and holes for Ru-CTFs.<sup>48</sup> The intensity of the emission band near 440 nm dropped  
277 significantly after addition of Ru(dcbpy)(CO)<sub>2</sub>Cl<sub>2</sub>, indicating that the Ru(dcbpy)(CO)<sub>2</sub>Cl<sub>2</sub> served as  
278 charge carrier trap centers to facilitate charge migration from the bulk to the interface of the polymer  
279 for reducing the recombination of photogenerated charges. Under UV light irradiation, the pure-  
280 CTF showed bright blue-green fluorescence (inset in Fig. 5e), consistent with the fluorescence  
281 emission spectrum.<sup>49</sup> In addition, time-resolved fluorescence (TRPL) spectra were recorded for all  
282 samples at an excitation wavelength of 375 nm (Fig. 5f). The decay kinetics of pure-CTF displayed

283 a shorter average lifetime (2.5 ns) than those of Ru-CTFs, confirming that the molecular Ru sites  
 284 can greatly enhance the separation of photogenerated charge carriers. The attenuated PL emission  
 285 and prolonged fluorescence lifetime of Ru-CTFs clearly reflected that the radiative recombination  
 286 of photoexcitons within this properly functionalized CTFs was effectively retarded.



287  
 288 **Fig. 5 Photoelectrochemical measurements.** (a) UV/Vis DRS spectra of CTFs with different  
 289 content of Ru. (b) Mott-Schottky plots for Ru-CTF, inset is the energy diagram of the CB and VB  
 290 levels of Ru-CTF. (c) Transient photocurrent response of all CTF materials under visible light  
 291 irradiation as indicated. (d) EIS Nyquist plots of CTFs conducted under visible light irradiation.  
 292 Steady-state PL emission spectra of CTFs in the solid state. (f) Time-resolved PL spectra of all CTF  
 293 materials in the solid state.

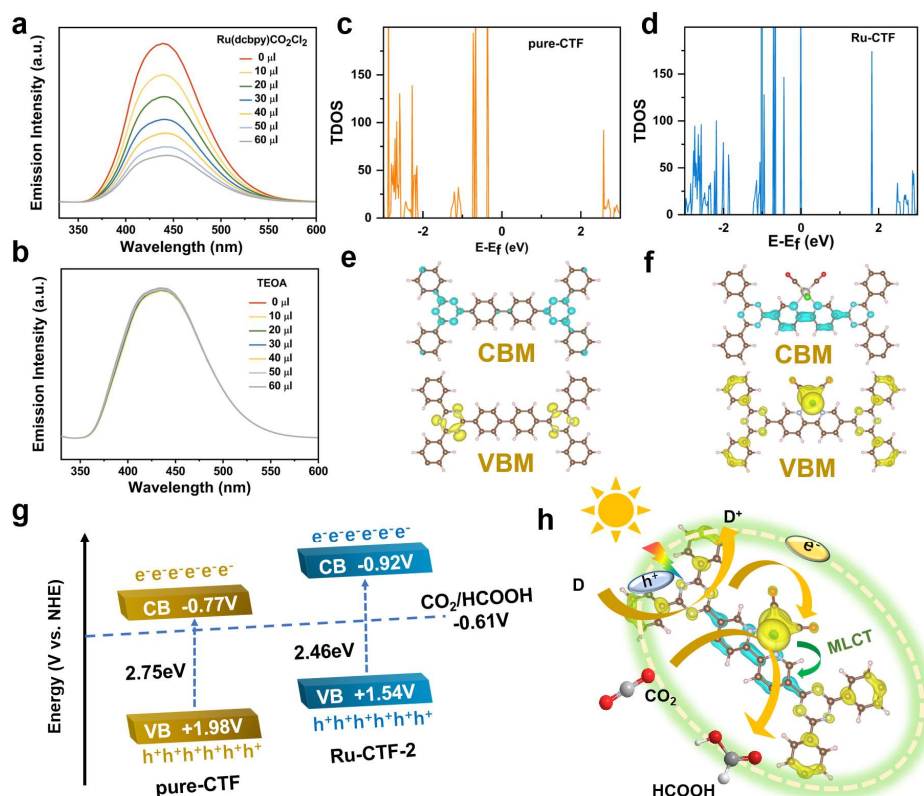
294 **Photocatalytic Mechanisms and Density Functional Theory (DFT) calculations.** To further  
 295 understand the role of the single-atom Ru sites in the photocatalytic CO<sub>2</sub>RR, photoluminescence  
 296 measurement of the catalytic system was performed. To demonstrate whether the excited CTF  
 297 support was reductively or oxidatively quenched by TEOA or Ru(dcbpy)(CO)<sub>2</sub>Cl<sub>2</sub> unit, respectively,  
 298 the luminescence quench experiments of CTF were studied with addition of TEOA and

299 Ru(dcbpy)(CO)<sub>2</sub>Cl<sub>2</sub>. As shown in Fig. 6a and b, the luminescence of CTF support was efficiently  
300 quenched by the Ru(dcbpy)(CO)<sub>2</sub>Cl<sub>2</sub> but not by TEOA. Therefore, these results indicate that the  
301 photocatalytic reduction of CO<sub>2</sub> process occurs via electron transfer from the photoexcited CTF  
302 support to the Ru unit, but not from TEOA to the excited CTF support, indicating an oxidative  
303 quenching mechanism in this photocatalytic process.<sup>3,50</sup> Then the oxidized CTF support was reduced  
304 by TEOA to complete the redox cycle. All the above results demonstrate that the integration of  
305 single-atom Ru unit with CTF support could effectively inhibit the recombination of photogenerated  
306 charge carriers and accelerate the electron transfer.

307 To reveal underlying the photocatalytic mechanism, we performed systematic DFT  
308 calculations to assess the electronic structures and possible reaction pathways in the pure-CTF and  
309 Ru-CTF systems. The fully relaxed structures were depicted in Supplementary Fig. 33. A two-  
310 dimension (2D) hexagonal periodicity was adopted for both the pure-CTF and the Ru-CTF, where  
311 the latter was constructed by substituting one of the biphenyl units with a Ru(dcbpy)(CO)<sub>2</sub>Cl<sub>2</sub>. The  
312 density of states (DOS) of pure-CTF and Ru-CTF were shown in Fig. 6c and d, respectively. The  
313 calculated band gaps of the pure-CTF and Ru-CTF systems are 2.93 and 2.48 eV, respectively  
314 (Supplementary Fig. 34), in consistent with the experimental values evaluated using the Tauc plot.  
315 We observed that the both the conduction band minimum (CBM) and the valence band maximum  
316 (VBM) in Ru-CTF lie much nearer to the Fermi level than those in pure-CTF, suggesting higher  
317 carrier density in Ru-CTF. The decrease of the band gap would facilitate the utilization efficiency  
318 of the visible light, and hence improve the CO<sub>2</sub>RR photocatalytic activity. Local density of states  
319 (LDOS) plots show that the band edge states localized on the CTF units for pure-CTF (Fig. 6e);  
320 while for Ru-CTF (Fig. 6f), both the CBM and the VBM were contributed by the Ru unit.  
321 Specifically, for Ru-CTF, the VBM and CBM located at the Ru unit and the dcbpy ligand,  
322 respectively, implying the Ru unit would be a good metal-to-ligand charge transfer (MLCT)  
323 acceptor-donor pair and would be feasible for electron-hole separation.

324 In light of the above experimental results and DFT calculations, the photocatalytic mechanism  
325 is proposed (Fig. 6g and h). A comprehensive analysis of the band gap and conduction band shows  
326 that the conduction band position of the pure-CTF catalyst is -0.77 V, while that of Ru-CTF is -0.92  
327 V, indicating that CO<sub>2</sub> is thermodynamically favorable to formic acid (-0.61 V vs. NHE). The  
328 possible charge-transfer pathway of the Ru-CTF is shown in Fig. 6h. Under visible light irradiation,  
329 the CTF support will be excited, which can transfer electron to the Ru unit, resulting in the  
330 separation of the photogenerated electron-hole pairs. In addition, a MLCT process could take place  
331 in the Ru unit according to the DRS results. The electrons at the Ru unit are used to reduce the  
332 adsorbed CO<sub>2</sub> molecule for HCOOH, which then dissolves in solution as HCOO<sup>-</sup>. Finally, the holes  
333 in the excited CTF support can be reduced by sacrificial donor (TEOA) to complete the catalytic

334 cycle. Additionally, the electron–hole separation and transfer processes were determined with a  
 335 combination of optical absorption spectra analysis and electrochemical measurements  
 336 (Supplementary Fig. 36).



337

338 **Fig. 6 Photocatalytic Mechanisms and Density Functional Theory (DFT) calculations.**

339 Photoluminescence spectra of the pure-CTF after the addition of different amounts of (a)  
 340 Ru(dcbpy)(CO)<sub>2</sub>Cl<sub>2</sub> and (b) TEOA in DMA with 320 nm excitation at room temperature. (c, d)  
 341 Corresponding total density of states (DOS) and (e, f) Local density of states (LDOS) plots of pure-  
 342 CTF and Ru-CTF estimated by DFT calculations, respectively. E<sub>f</sub> refers to “Fermi level” that is the  
 343 center between CB and VB. (g) The band diagram of the pure-CTF and the Ru-CTF catalysts. (h)  
 344 The mechanism of photoreduction CO<sub>2</sub> by the Ru-CTF catalyst.

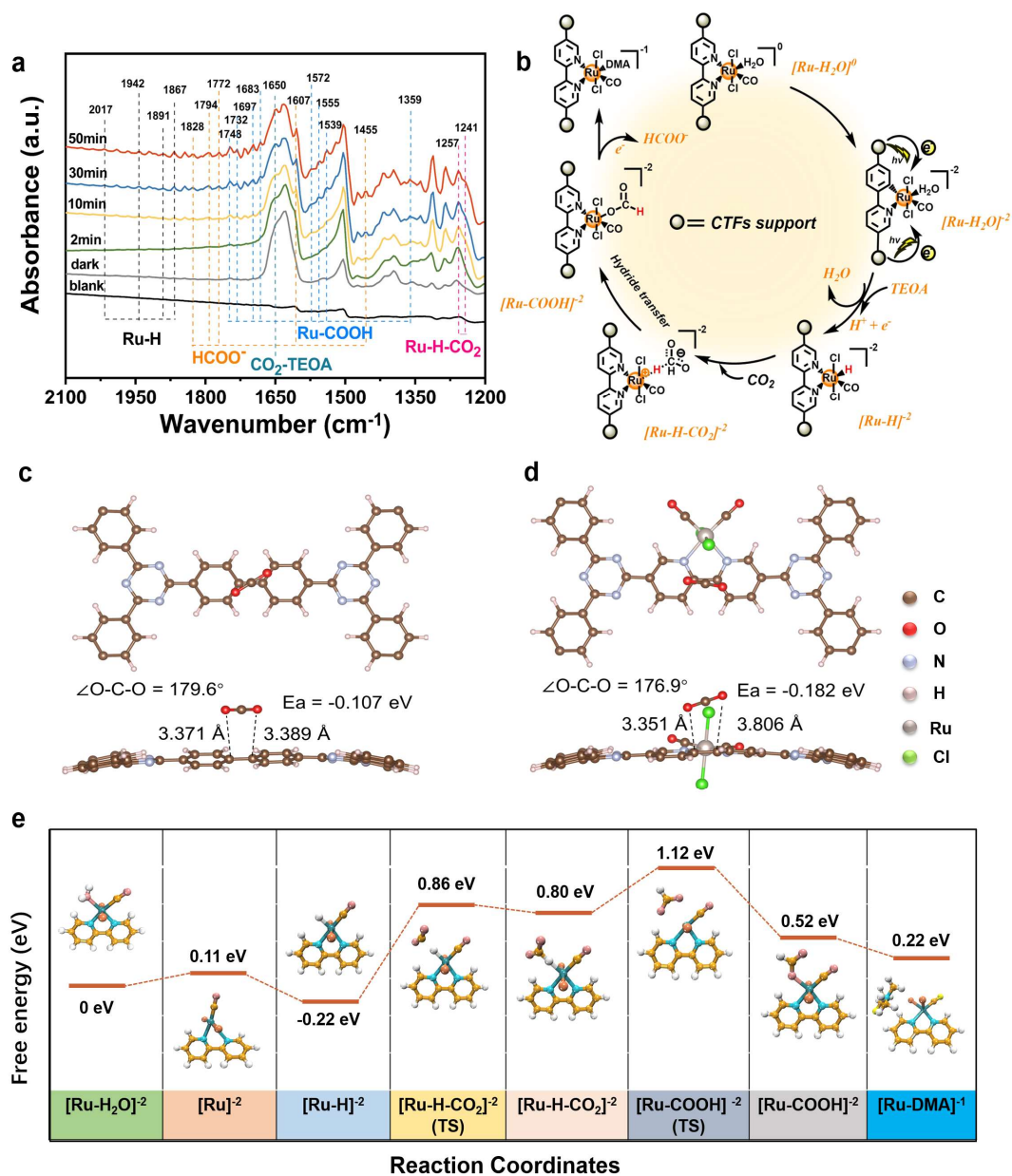
345 **Reaction Mechanisms of CO<sub>2</sub> to HCOO<sup>-</sup> on the single-atom Ru Site.**

346 To probe the reaction intermediates in the photocatalytic reaction, the *in-situ* attenuated total reflection-infrared (ATR-IR)  
 347 spectroscopy was investigated. The *in-situ* ATR-IR spectra of the photocatalytic reaction recorded  
 348 without addition of the catalyst were selected as the background, then, all the subsequent ATR-IR  
 349 spectra were recorded by subtracting the background (Supplementary Fig. 37). As the range from  
 350 1200 to 2100 cm<sup>-1</sup> contains a lot of carbonaceous species information, a three-dimensional zoomed-  
 351 in perspective of this region is shown in Supplementary Fig. 37 and the obvious change can be seen  
 352 from the figure, then several spectral lines were selected for specific analysis (Fig. 7a). As shown in

353 Fig. 7a, the carbonyl stretch peak at  $1650\text{ cm}^{-1}$  was gradually strengthened with the increase of the  
354 irradiation time. This can be ascribed to the fact that  $\text{CO}_2$  may react with TEOA to form a  
355 zwitterionic alkylcarbonate ( $\text{CO}_2\text{-TEOA}$ , Supplementary Fig. 38).<sup>51</sup> Notably, the major species  
356 observable by IR correspond to metal hydride Ru-H at  $2017, 1942, 1891$  and  $1867\text{ cm}^{-1}$ , consistent  
357 with previous reports.<sup>51,52</sup> In addition, the  $\text{CO}_2$  coordinated to the metal hydride Ru-H resulted in  
358 the quick formation of Ru-H- $\text{CO}_2$  species, corresponding to the peaks from  $1240$  to  $1270\text{ cm}^{-1}$   
359 ascribed to the  $\text{CO}_2$  coordinated to the metal hydride.<sup>42</sup> The emergence of the peak at  $1257\text{ cm}^{-1}$   
360 over  $\text{CO}_2$ -saturated Ru-CTF suggests the direct adsorption of  $\text{CO}_2$  onto the Ru-H center.<sup>53</sup> The H-  
361 bound formate intermediate followed by rotational rearrangement to generate the O-bound formate  
362 product (Ru-COOH).<sup>51</sup> The peaks at  $1359, 1539, 1555, 1572, 1683, 1697, 1732$  and  $1748\text{ cm}^{-1}$   
363 corresponding to Ru-COOH also increased as time went on, demonstrating that Ru-COOH is a  
364 crucial intermediate for the photo-reduced conversion of  $\text{CO}_2$  to formic acid.<sup>36,38,48,54,55</sup> Moreover,  
365 the peaks at  $1455, 1607, 1772, 1794$  and  $1828\text{ cm}^{-1}$  are ascribed to formate ion ( $\text{HCOO}^-$ ).<sup>42,56</sup>

366 A detailed and thorough mechanistic pathway over the Ru- $\text{N}_2$  site in Ru-CTF was proposed for  
367 better understanding the reaction thermodynamics based on DFT calculations. As shown in Fig. 7c,  
368 d and Supplementary Fig. 39, the introduction of Ru and N site in  $\text{Ru}(\text{dcbpy})(\text{CO})_2\text{Cl}_2$  molecular  
369 could enhance the material's absorption of  $\text{CO}_2$ , and notably, the linear structure of  $\text{CO}_2$  was also  
370 bent, indicating that  $\text{Ru}(\text{dcbpy})(\text{CO})_2\text{Cl}_2$  molecular had a strong ability to activate  $\text{CO}_2$ , which was  
371 beneficial to start the entire reaction. Additionally, the improved  $\text{CO}_2$  adsorption capacity for Ru-  
372 CTF was in consistent with the volumetric  $\text{CO}_2$  adsorption measurements. Furthermore, the relative  
373 Gibbs free energy ( $\Delta G$ ) diagram (Fig. 7e) along with detailed mechanistic pathway (Fig. 7b) was  
374 constructed by using DFT calculations based on the information obtained from *in-situ* ATR-IR (Fig.  
375 7a). Significantly, according to the results of XAFS measurements, one of the carbonyl ligands in  
376 Ru-CTF was substituted by a  $\text{H}_2\text{O}$  molecule. Furthermore, the exited CTF support could be  
377 oxidatively quenched by Ru unit to drive the  $[\text{Ru-H}_2\text{O}]^0$  to generate  $[\text{Ru-H}_2\text{O}]^{-2}$ .<sup>52,57,58</sup> Followed a  
378  $[\text{H}_2\text{O}]$  loss and reacts with  $\text{H}^+$  and  $\text{e}^-$  to generate metal hydride  $[\text{Ru-H}]^{-2}$ .<sup>51,59</sup> In the process of  $\text{CO}_2\text{RR}$ ,  
379 the metal hydride  $[\text{Ru-H}]^{-2}$  intermediate was more likely to form through the substitution of  $\text{H}_2\text{O}$   
380 site ( $\Delta G = -0.33\text{ eV}$ ) rather than the substitution of chlorine (Cl) ( $\Delta G = +2.49\text{ eV}$ ) in Ru-CTF (details  
381 in Supplementary Fig. 40). Moreover, TEOA was the proton and electron source for metal hydride  
382 generation.<sup>51</sup> The metal hydride can react with  $\text{CO}_2$  to generate a  $[\text{Ru-H-CO}_2]^{-2}$  adduct.<sup>51,58</sup> The  
383 formation of the  $[\text{Ru-H-CO}_2]^{-2}(\text{TS})$  intermediates was found to be the rate-limiting step for  $\text{CO}_2$  to  
384  $\text{HCOO}^-$ . The H-bound formate intermediate  $[\text{Ru-H-CO}_2]^{-2}$  was transiently formed after the  
385 nucleophilic attack of  $\text{CO}_2$  by the metal hydride, followed by rotational rearrangement to generate  
386 the O-bound highly stable  $[\text{Ru-COOH}]^{-2}$  intermediate ( $\Delta G = -0.28\text{ eV}$ ). Finally, the  $\text{HCOO}^-$  can be  
387 released by cleaving the Ru-O bond to recover the initial state. The remaining exited CTF support

388 from the oxidative quenching pathway can be reduced to original state by TEOA, completing the  
 389 photocatalytic cycle.<sup>51,57</sup> High thermodynamic feasibility of almost all the intermediate steps as  
 390 revealed from the relative Gibbs free energy calculations successfully explained the exceptionally  
 391 high catalytic activity of Ru-CTF as a visible-light-driven photocatalyst for CO<sub>2</sub>RR.



392

393 **Fig. 7 Reaction Mechanisms of CO<sub>2</sub> to HCOO<sup>-</sup> on the single-atom Ru Site.** (a) *In-situ* attenuated  
 394 total reflection-infrared (ATR-IR) of Ru-CTF samples in specific analysis. (b) Proposed catalytic  
 395 mechanism with the molecular unit of Ru for photocatalytic CO<sub>2</sub> reduction to HCOOH.  
 396 Adsorption energy of CO<sub>2</sub> on (c) pure-CTF and (d) Ru-CTF surface. (e) Gibbs free energy pathway  
 397 for the formation of HCOO<sup>-</sup> from CO<sub>2</sub>.

398

## 399 **Conclusions**

400 In summary, the *in-situ* knitting of well-defined single-site catalysts into extended frameworks  
401 (CTFs) to construct efficient heterogeneous catalysts for photocatalytic CO<sub>2</sub> reduction to HCOOH  
402 has been successfully created via a new strategy for the first time, which can not only maintain good  
403 photoresponsive performances of CTFs but also firmly anchor and atomically disperse Ru site. The  
404 precise coordination structure of the well-defined Ru-N<sub>2</sub> sites in CTFs have been characterized and  
405 analyzed by using EXAFS analysis. Significantly, the resulting single-site Ru-CTF can serve as  
406 efficient platform to bridge the gap between homogeneous molecular catalysts and heterogeneous  
407 catalysts, greatly contributing to the excellent activity, selectivity and stability for the CO<sub>2</sub>  
408 photoreduction. The improved CO<sub>2</sub> uptake capacity in the Ru-CTF could interact better with CO<sub>2</sub>,  
409 thus enhancing the photocatalytic CO<sub>2</sub> reduction. Moreover, it has been found that single-site Ru  
410 knitted into stable CTFs can promote the separation of photogenerated electrons-holes, thus  
411 boosting the activity of photoreduction, which exceeds most of the previously reported  
412 photocatalytic systems. Notably, Ru-CTF also exhibits noteworthy recyclability, revealing the  
413 robust stability with the extended reaction duration. In addition, systematic DFT calculations were  
414 used to assess the electronic structures and possible reaction pathways. Our study offers a new  
415 approach toward the rational design and preparation of molecularly precise photocatalysts for  
416 efficient solar-to-fuel energy conversion, in addition, we believe that the *in-situ* knitting strategy of  
417 CTFs hold enormous potential for energy-related photocatalysis.

## 418 **Methods**

419 **Chemicals.** All reagents, unless otherwise stated, were obtained from commercial sources and were  
420 used without further purification. Specifically, 2,2'-bipyridine-5,5'-dicyanitrile (dcbpy, 97%), 4,4'-  
421 biphenyldicarbonitrile (dcbph, 97%), ruthenium(III) chloride trihydrate (RuCl<sub>3</sub> · 3H<sub>2</sub>O, 99.9%),  
422 trifluoromethanesulfonic acid (CF<sub>3</sub>SO<sub>3</sub>H, 98%) and paraformaldehyde ((CH<sub>2</sub>O)<sub>n</sub>, AR) were  
423 purchased from Aladdin. Formic acid (88%), hexane, dichloromethane, ammonia solution (25-28  
424 vol%), *N,N*-dimethylacetamide (DMA, HPLC), triethanolamine (TEOA, HPLC 99.5%) and  
425 methanol (HPLC) were purchased from Sinopharm Chemical Reagent Co. Ltd. *N,N*-  
426 dimethylacetamide (DMA) and TEOA were dried over 4 Å molecular sieves for several days. DMA  
427 and TEOA were kept under Ar prior to use.

428 **Synthesis of [Ru(CO)<sub>2</sub>Cl<sub>2</sub>]<sub>n</sub>.** [Ru(CO)<sub>2</sub>Cl<sub>2</sub>]<sub>n</sub> was synthesized based on previously reported  
429 methods.<sup>58,60</sup> RuCl<sub>3</sub> · 3H<sub>2</sub>O (0.522 g) and paraformaldehyde (0.206 g) were added to an argon-  
430 degassed solution of formic acid (88%, 40 ml). Then the solution mixture was heated to reflux for  
431 12 h. After cooling to room temperature, the mixture was stored at 4 °C overnight for complete  
432 conversion to the [Ru(CO)<sub>2</sub>Cl<sub>2</sub>]<sub>n</sub> polymer. The product was obtained by removing the solvent under

433 vacuum, which was washed twice with hexane ( $2 \times 50$  ml) and dried under vacuum to obtain a  
434 bright yellow solid (yield, 56%). IR(Nujol):  $\nu_{\text{co}}$  at 2072 and 2011  $\text{cm}^{-1}$  ( $\nu_{\text{co}}$  at 2146  $\text{cm}^{-1}$  for the  
435 orange dimer  $[\text{Ru}(\text{CO})_3\text{Cl}_2]_2$ , which may occur as an impurity).

436 **Synthesis of  $[\text{Ru}(\text{dcbpy})(\text{CO})_2\text{Cl}_2]$ .**  $[\text{Ru}(\text{dcbpy})(\text{CO})_2\text{Cl}_2]$  was synthesized based on previously  
437 reported methods.<sup>60-61</sup> In a typical experiment, 2,2'-bipyridine-5,5'-dicyanitrile (0.103 g, 0.5 mmol)  
438 was mixed with methanol (25 mL) under  $\text{N}_2$  for 30 min, then  $[\text{Ru}(\text{CO})_2\text{Cl}_2]_n$  (0.114 g, 0.5 mmol)  
439 was added and heated at reflux under the inert atmosphere for 3 h with vigorous stirring in dark.  
440 After standing overnight at 4 °C for complete precipitation of the product, the precipitate was  
441 filtered onto a glass frit and washed twice with cold methanol ( $2 \times 50$  ml) and finally washed several  
442 times with a small amount of dichloromethane ( $6 \times 0.5$  ml) in dark.  $[\text{Ru}(\text{dcbpy})(\text{CO})_2\text{Cl}_2]$  was  
443 collected after being dried in a vacuum desiccator (yield, 47%). This product should be sealed in  
444 argon cool dry place away from light.

445 **Synthesis of Ru-CTFs.** Covalent triazine frameworks (CTFs) were prepared by using tri-  
446 fluoromethanesulfonic acid ( $\text{CF}_3\text{SO}_3\text{H}$ ) as the catalyst.<sup>17,30,31,49,62</sup>  $[\text{Ru}(\text{dcbpy})(\text{CO})_2\text{Cl}_2]$  (0.0108 g,  
447 0.025 mmol) and 4,4'-biphenyldicyanitrile (0.1174 g, 0.575 mmol) were added into a pre-dried  
448 flask, then 3.24 g (21.6 mmol) of  $\text{CF}_3\text{SO}_3\text{H}$  was added under nitrogen at 0 °C. The obtained orange  
449 red solution was then stirred for 1 h to completely dissolve the monomers before the heating  
450 treatment of 120 °C for 10 min. The solution was then warmed at 100 °C and kept stirring at this  
451 temperature for 2 h to initiate the trimerization reaction of terminal cyano groups and form the Ru-  
452 CTF oligomer. Then the solution was further stirred under the temperature of 80 °C for 10 h to allow  
453 complete conversion to the polymer. The obtained deep red solution was then quenched by ethanol  
454 for obtaining the precipitated golden solid (Supplementary Fig. 3). After that, the mixture was  
455 poured into 160 mL of water containing 25 mL of ammonia solution and stirred for 2 h. Notably,  
456 the suspension changed color from golden yellow to red-brown (Supplementary Fig. 3). The  
457 precipitates were filtered and further purified by Soxhlet extraction with ethanol, methanol and  
458 dichloromethane, respectively. Finally, the obtained red-brown solid was grounded into powder with  
459 an agate mortar, which should be sealed in argon cool dry place away from light (63% yield). Ru-  
460 CTF with various loading amounts of  $[\text{Ru}(\text{dcbpy})(\text{CO})_2\text{Cl}_2]$  were denoted as Ru-CTF-3, Ru-CTF-2,  
461 Ru-CTF-1 (Supplementary Fig. 4). The pure-CTF was prepared by the same method without  
462 addition of  $[\text{Ru}(\text{dcbpy})(\text{CO})_2\text{Cl}_2]$ .

463 **Characterization.** Scanning electron microscopy (SEM) images were obtained with a Hitachi  
464 SU8010 microscope. Energy-dispersive X-ray spectroscopy (EDX) mapping images were obtained  
465 using a TESCAN MIRA3 FEG-SEM instrument with an Oxford Instruments Aztec Energy X-maxN  
466 80 system at an acceleration voltage of 15 kV. Raman spectra were measured on a Raman  
467 spectrometer Labram HR evolution (Horiba JobinYvon, France), using a 532 nm excitation laser,

468 between 100 and 3500  $\text{cm}^{-1}$ . X-ray photoelectron spectra (XPS) were performed using a Thermo  
469 scientific XPS K-alpha 250Xi surface analysis machine using an Al source. Analysis was performed  
470 using XPS Peak 4.1 software. All binding energies were referenced to the C1s peak (284.6 eV) of  
471 the surface adventitious carbon.<sup>63,43</sup> Thermogravimetric analysis (TGA) was carried out on  
472 TAsDT650 (TA Instruments, USA) by heating the samples from 40 to 1000 °C under nitrogen flow  
473 (100 mL/min) with a heating rate of 10 °C/min. N<sub>2</sub> and CO<sub>2</sub> adsorption isotherms were collected on  
474 a Quantachrome Instruments Autosorb-iQ (Boynton Beach, Florida USA) with extra-high pure  
475 gases at 77 K and 273 K from 0 to 1 atm, respectively. The samples were activated before adsorption  
476 measurements. The fresh as-synthesized samples (~50 mg) were activated by heating under a  
477 dynamic vacuum at 150 °C for 10 h. Before the gas adsorption test, the samples need to be dried  
478 again by using the outgas function of the surface area analyzer for 12 h at 150 °C. UV-Vis diffused  
479 reflectance spectra (DRS) were measured on a spectrometer (UV-2700, Shimadzu, Japan) by  
480 measuring the reflectance of powders in the solid state using barium sulfate (BaSO<sub>4</sub>) as a standard  
481 with 100% reflectance. The scan was arranged from 190 to 900 nm with the scan rate of medium.  
482 Powder X-ray diffraction (PXRD) patterns were recorded on a Bruker D8 diffractometer (German)  
483 equipped with Cu/K $\alpha$  radiation ( $\lambda = 1.5418 \text{ \AA}$ ) under a scan rate of 5 degree/min. The sample was  
484 spread on the circular recess of silicon holder as a thin layer. Metal content analyse was obtained by  
485 inductively coupled plasma-atomic emission spectrometry (ICP-AES) using the iCAP 7400  
486 spectrometer (Thermo Fisher Scientific, USA). Heterogeneous samples were preprocessed by acid  
487 digestion with concentrated nitric acid. <sup>1</sup>H and <sup>13</sup>C NMR spectra were recorded in solution using a  
488 Bruker Advance 400 NMR spectrometer. Fourier-transform infrared spectra (FTIR) were collected  
489 on a Shimadzu IRTracer-100 FT-IR spectrometer in attenuated total reflection (ATR) infrared mode  
490 at a resolution of 4  $\text{cm}^{-1}$  and averaging 45 scans. The samples were compressed on a ZnSe window.  
491 **Photoluminescence (PL) spectra and decay curve.** The steady-state photoluminescence (PL)  
492 emission spectra of CTFs were measured in the solid state by the HITACHI F-7000 PL spectrometer  
493 using a 320 nm laser as the excitation source at room temperature. Samples were placed in a hole at  
494 the center of a plate-S5 type cell, then CTFs were exposed to laser source, and the data were  
495 collected at the emission peak of the corresponding CTFs. Time-resolved fluorescence spectra for  
496 CTFs were obtained by a time-correlated single photon counting (TCSPC) method using an  
497 Edinburgh Instruments FL920 spectrofluorometer equipped with 375 nm laser for excitation light  
498 source. A detection wavelength of 445 nm was used for all CTFs samples.  
499 ***In-situ* attenuated total reflection-infrared (ATR-IR).** The *in-situ* attenuated total reflection-  
500 infrared (ATR-IR) spectroscopy was performed on Shimadzu IRTracer-100 equipped with a single  
501 reflection silicon ATR module and IR cell (Supplementary Fig. 1) with IR incidence at 45 degrees.  
502 Firstly, the sample was treated under dynamic vacuum at 80 °C for 2 h. Then the solution with a

503 catalyst was purged with CO<sub>2</sub> (99.999%), after reaching adsorption equilibrium, an ATR-IR  
504 spectrum was collected. The solutions for photocatalytic CO<sub>2</sub> conversion were irradiated by a 300  
505 W Xe-lamp (FX300, Beijing Perfect Light Technology Co., Ltd., Beijing, China). And in order to  
506 prevent evaporation of solvent and provide good light transmission, liquid samples kept covered  
507 with quartz. The ATR-IR spectra were recorded every 2 min at the resolution of 8 cm<sup>-1</sup> and 150  
508 scans.

### 509 **X-ray absorption measurements (XAFS) and analysis.**

510 **XAFS measurements.** The X-ray absorption fine structure spectra (XAFS) were studied in X-ray  
511 absorption near edge structure (XANES) and extended X-ray absorption fine structure (EXAFS)  
512 regions for Ru. The Ru K-edge XAFS were collected at BL14W1 beamline of Shanghai Synchrotron  
513 Radiation Facility (SSRF). The data were collected in transmission mode or fluorescence mode  
514 using a Lytle detector while the corresponding reference sample were collected in transmission  
515 mode. All samples were grinded and uniformly daubed on 3M Kapton Polyimide tape (purchased  
516 from 3M).

517 **XAFS Analysis and Results.** The acquired EXAFS data were processed according to the standard  
518 procedures using the ATHENA module of Demeter software packages. The EXAFS spectra were  
519 obtained by subtracting the post-edge background from the overall absorption and then normalizing  
520 with respect to the edge-jump step. Subsequently, the  $\chi(k)$  data of were Fourier transformed to real  
521 (R) space using a window ( $dk=1.0 \text{ \AA}^{-1}$ ) to separate the EXAFS contributions from different  
522 coordination shells. To obtain the quantitative structural parameters around central atoms, least-  
523 squares curve parameter fitting was performed using the ARTEMIS module of Demeter software  
524 packages

525 The following EXAFS equation was used:

526

$$527 \quad \chi(k) = \sum_j \frac{N_j S_0^2 F_j(k)}{k R_j^2} \cdot \exp[-2k^2 \sigma_j^2] \cdot \exp\left[\frac{-2R_j}{\lambda(k)}\right] \cdot \sin[2kR_j + \phi_j(k)]$$

528 the theoretical scattering amplitudes, phase shifts and the photoelectron mean free path for all paths  
529 calculated.  $S_0^2$  is the amplitude reduction factor,  $F_j(k)$  is the effective curved-wave backscattering  
530 amplitude,  $N_j$  is the number of neighbors in the  $j^{\text{th}}$  atomic shell,  $R_j$  is the distance between the X-ray  
531 absorbing central atom and the atoms in the  $j^{\text{th}}$  atomic shell (backscatterer),  $\lambda$  is the mean free path  
532 in  $\text{\AA}$ ,  $\phi_j(k)$  is the phase shift (including the phase shift for each shell and the total central atom phase  
533 shift),  $\sigma_j$  is the Debye-Waller parameter of the  $j^{\text{th}}$  atomic shell (variation of distances around the  
534 average  $R_j$ ). The functions  $F_j(k)$ ,  $\lambda$  and  $\phi_j(k)$  were calculated with the ab initio code FEFF9. The  
535 additional details for EXAFS simulations are given below.

536 All fits were performed in the  $R$  space with  $k$ -weight of 2 while phase correction was also

537 applied in the first coordination shell to make R value close to the physical interatomic distance  
538 between the absorber and shell scatterer. The coordination numbers of model samples were fixed as  
539 the nominal values. While the  $S_0^2$ , internal atomic distances R, Debye-Waller factor  $\sigma^2$ , and the  
540 edge-energy shift  $\Delta$  were allowed to run freely.

541 **Photoelectrochemical measurements.** The Mott-Schottky (M-S) measurements, electrochemistry  
542 impedance spectroscopy (EIS) and transient photocurrent (TPC) response measurements were  
543 measured via a CHI 660E electrochemical station (Shanghai Chenhua Co.) in a standard three  
544 electrode configuration. The Pt plate served as the counter electrode, a saturated Ag/AgCl electrode  
545 as a reference electrode, indium tin oxides (ITO) conductive glass was used as the conductive  
546 substrate to prepare the working electrode. The details are as below: 10 mg CTFs were dispersed in  
547 a mixed solution of 0.2 mL ethanol containing 20  $\mu$ L 5 wt% Nafion D-520, and then were sonicated  
548 10 min to generate a homogeneous slurry. Subsequently, 60  $\mu$ L slurry was coated on the ITO glass  
549 substrate with the area  $1 \times 1$  cm<sup>2</sup>, and then dried at 60 °C in vacuum oven for 12 h. 0.2 M Na<sub>2</sub>SO<sub>4</sub>  
550 aqueous solution was used as the electrolyte. The Mott-Schottky analysis was conducted in the dark  
551 at the frequency of 500, 1000 and 1500 Hz. The transient photocurrent was conducted under visible  
552 light irradiation with the fixed time interval. A 300 W Xenon lamp (Beijing PerfectLight Co. Ltd.,  
553 PLS-SXE300) with a 400 nm cut-off filter was used as the light source in the photocurrent (TPC)  
554 response measurement. EIS analysis was performed at the open circuit condition at the frequency  
555 range from 0.01 to 100000 Hz. The EIS under the conditions of dark and light excitation was  
556 acquired.

557 **Photocatalytic measurement of CO<sub>2</sub> reduction.** The photocatalytic CO<sub>2</sub> reduction experiments  
558 were carried in Parallel Light Reactor (WP-TEC-1020HSL, WATTCAS, China) (Supplementary  
559 Fig. 2). Before the CO<sub>2</sub> reduction, these samples were activated by heating under a dynamic vacuum  
560 at 60 °C for 6 h to form the activated samples. After activation, samples for CO<sub>2</sub> reduction were  
561 prepared in a 20 mL quartz tube. Each photocatalytic process includes 0.5 mg of Ru-CTF, 0.75 mL  
562 of DMA, and 0.25 mL of TEOA (triethanolamine). Then the vessel was sealed with a rubber stopper.  
563 The mixture was purged with CO<sub>2</sub> (99.999%) by evacuated and backfilled CO<sub>2</sub> three times to  
564 remove air before irradiation. Next, the reaction mixture was vigorously stirred to ensure the  
565 photocatalyst particles in suspension, and a LED lamp (8 W) was served as the visible light source  
566 by bottom-irradiation. The intensity of the incident light on the solution surface was about 258  
567 mW/cm<sup>2</sup>, which was measured on a spectroradiometer (PCS230580, WATTCAS, China). The  
568 irradiated surface area of the solution is about 3.14 cm<sup>2</sup>. The distance between the vent of the lamp  
569 and the bottom of the reactor was about 0.5 cm. All tests of the photocatalytic reaction were  
570 performed under the same conditions. The temperature of the solution was maintained at 20 °C  
571 using a circulating cooling water system during irradiation. After completion of the reaction, the

572 amount of HCOOH was measured by high-performance liquid chromatography HPLC system (LC-  
573 2030 Plus, Shimadzu, Japan) at wavelength of 210 nm with 20 mM H<sub>3</sub>PO<sub>4</sub> as the mobile phase.  
574 Gaseous product was measured by gas chromatography (GC-2014, Shimadzu, Japan) equipped with  
575 a flame ionization detector (FID) and a thermal conductivity (TCD).

576 **Recycling experiments.** All the Ru-CTF catalysts were isolated by centrifuging from the mixture,  
577 and washed with DMA for 3 times, then redispersed Ru-CTF in DMA to run photocatalytic reaction  
578 again under the same condition mentioned above.

579 **Computational details.** To assess the effect of Ru(dcbpy)(CO)<sub>2</sub>Cl<sub>2</sub> substitution on the electronic  
580 structures of the CTF, we adopted an extended model with two-dimensional periodicity in the  
581 molecular plane. In this part, all the calculations were carried out by using density functional theory  
582 with the projector-augmented wave method and the Perdew-Burke-Ernzerhof (PBE) exchange-  
583 correlation function implemented in the VASP package. The dispersion corrected DFT-D3 scheme  
584 was used to account for the dispersion interactions. The pseudo wavefunctions were expanded in  
585 the space spanned by plane-waves with kinetic energy cutoff of 500 eV. The energy and force  
586 convergence criteria were set to 10<sup>-6</sup> eV and 0.02 eV/Å, respectively. A hexagonal symmetry was  
587 adopted to construct the periodic model, containing Ru atoms in a 1 × 1 unit cell, respectively, for  
588 the pristine (Ru(dcbpy)(CO)<sub>2</sub>Cl<sub>2</sub> substituted) systems. A vacuum layer of 20 Å was padded in the  
589 normal direction of the system, to avoid interactions between neighboring layers. Due to the large  
590 size of the unit cell, we used KGRID-MESH for structure relaxation, and with a Ru(dcbpy)(CO)<sub>2</sub>Cl<sub>2</sub>  
591 for electronic structure calculation.

592 The catalytic reaction activity was assessed by DFT calculations with constraint models, where  
593 the electron-electron interactions were described with the hybrid B3LYP/M06 functional  
594 implemented in the Gaussian 16 package. The moderate size basis set 6-31G\* was used in structure  
595 optimization and frequency analysis, while the energetics and electronic structures were calculated  
596 with a much larger basis set 6-311++G basis set on the optimized structures. The LANL08  
597 relativistic effective core potential and basis set were used for the Ru atoms. In all the calculations,  
598 the self-consistent reaction field method with the polarizable continuum model (SCRF-PCM) was  
599 used to implicitly account for the solvent effects.

## 600 **Data availability**

601 The data that support the plots within this paper and other findings are available from the  
602 corresponding author upon reasonable request.

## 603 **References**

604 1 Shih, C. F., Zhang, T., Li, J. & Bai, C. Powering the Future with Liquid Sunshine. *Joule* **2**,  
605 1925-1949 (2018).

- 606 2 Hull, J. F. *et al.* Reversible hydrogen storage using CO<sub>2</sub> and a proton-switchable iridium  
607 catalyst in aqueous media under mild temperatures and pressures. *Nature Chem* **4**, 383-388  
608 (2012).
- 609 3 Yan, Z.-H. *et al.* Photo-generated dinuclear {Eu(II)}<sub>2</sub> active sites for selective CO<sub>2</sub>  
610 reduction in a photosensitizing metal-organic framework. *Nature Communications* **9**, 3353  
611 (2018).
- 612 4 Enthaler, S., von Langermann, J. & Schmidt, T. Carbon dioxide and formic acid—the  
613 couple for environmental-friendly hydrogen storage? *Energy Environ Sci* **3**, 1207-1217  
614 (2010).
- 615 5 Han, N., Ding, P., He, L., Li, Y. & Li, Y. Promises of Main Group Metal-Based  
616 Nanostructured Materials for Electrochemical CO<sub>2</sub> Reduction to Formate. *Advanced*  
617 *Energy Materials* **10**, 1902338 (2020).
- 618 6 Kuriki, R., Sekizawa, K., Ishitani, O. & Maeda, K. Visible-Light-Driven CO<sub>2</sub> Reduction  
619 with Carbon Nitride: Enhancing the Activity of Ruthenium Catalysts. *Angew Chem Int Ed*  
620 **54**, 2406-2409 (2015).
- 621 7 Sato, S., Morikawa, T., Saeki, S., Kajino, T. & Motohiro, T. Visible-Light-Induced Selective  
622 CO<sub>2</sub> Reduction Utilizing a Ruthenium Complex Electrocatalyst Linked to a p-Type  
623 Nitrogen-Doped Ta<sub>2</sub>O<sub>5</sub> Semiconductor. *Angew Chem Int Ed* **49**, 5101-5105 (2010).
- 624 8 Sekizawa, K., Sato, S., Arai, T. & Morikawa, T. Solar-Driven Photocatalytic CO<sub>2</sub> Reduction  
625 in Water Utilizing a Ruthenium Complex Catalyst on p-Type Fe<sub>2</sub>O<sub>3</sub> with a  
626 Multiheterojunction. *ACS Catal.* **8**, 1405-1416 (2018).
- 627 9 Kuriki, R. *et al.* Nature-Inspired, Highly Durable CO<sub>2</sub> Reduction System Consisting of a  
628 Binuclear Ruthenium(II) Complex and an Organic Semiconductor Using Visible Light. *J.*  
629 *Am. Chem. Soc.* **138**, 5159-5170 (2016).
- 630 10 Kuriki, R. *et al.* Robust Binding between Carbon Nitride Nanosheets and a Binuclear  
631 Ruthenium(II) Complex Enabling Durable, Selective CO<sub>2</sub> Reduction under Visible Light  
632 in Aqueous Solution. *Angew Chem Int Ed* **56**, 4867-4871 (2017).
- 633 11 Kuhn, P., Antonietti, M. & Thomas, A. Porous, Covalent Triazine-Based Frameworks  
634 Prepared by Ionothermal Synthesis. *Angew Chem Int Ed* **47**, 3450-3453 (2008).
- 635 12 Sakaushi, K. & Antonietti, M. Carbon- and Nitrogen-Based Organic Frameworks. *Accounts*  
636 *Chem Res* **48**, 1591-1600 (2015).
- 637 13 Lu, C. *et al.* Atomic Ni Anchored Covalent Triazine Framework as High Efficient  
638 Electrocatalyst for Carbon Dioxide Conversion. *Adv Funct Mater* **29**, 1806884 (2019).
- 639 14 Wang, Y. *et al.* Construction of Fully Conjugated Covalent Organic Frameworks via Facile  
640 Linkage Conversion for Efficient Photoenzymatic Catalysis. *J. Am. Chem. Soc.* **142**, 5958-  
641 5963 (2020).
- 642 15 Zhang, G., Lan, Z.-A. & Wang, X. Conjugated Polymers: Catalysts for Photocatalytic  
643 Hydrogen Evolution. *Angew Chem Int Ed* **55**, 15712-15727 (2016).
- 644 16 Liu, M., Guo, L., Jin, S. & Tan, B. Covalent triazine frameworks: synthesis and applications.  
645 *J. Mater. Chem. A* **7**, 5153-5172 (2019).
- 646 17 Lan, Z.-A., Fang, Y., Zhang, Y. & Wang, X. Photocatalytic Oxygen Evolution from  
647 Functional Triazine-Based Polymers with Tunable Band Structures. *Angew Chem Int Ed*  
648 **57**, 470-474 (2018).
- 649 18 Wang, G.-B. *et al.* Covalent organic frameworks: emerging high-performance platforms for

650 efficient photocatalytic applications. *J. Mater. Chem. A* **8**, 6957-6983 (2020).

651 19 Johnson, E. M., Haiges, R. & Marinescu, S. C. Covalent-Organic Frameworks Composed  
652 of Rhenium Bipyridine and Metal Porphyrins: Designing Heterobimetallic Frameworks  
653 with Two Distinct Metal Sites. *Acs Appl Mater Interfaces* **10**, 37919-37927 (2018).

654 20 Li, R., Zhang, W. & Zhou, K. Metal–Organic-Framework-Based Catalysts for  
655 Photoreduction of CO<sub>2</sub>. *Adv Mater* **30**, 1705512 (2018).

656 21 Cortes, S., Brucher, E., Geraldes, C. F. G. C. & Sherry, A. D. Potentiometry and NMR  
657 studies of 1,5,9-triazacyclododecane-N,N',N''-triacetic acid and its metal ion complexes.  
658 *Inorg Chem* **29**, 5-9 (1990).

659 22 Maeda, K. *et al.* Visible-light CO<sub>2</sub> reduction over a ruthenium(ii)-complex/C<sub>3</sub>N<sub>4</sub> hybrid  
660 photocatalyst: the promotional effect of silver species. *J. Mater. Chem. A* **6**, 9708-9715  
661 (2018).

662 23 Preti, D., Squarcialupi, S. & Fachinetti, G. Production of HCOOH/NEt<sub>3</sub> Adducts by CO<sub>2</sub>/H<sub>2</sub>  
663 Incorporation into Neat NEt<sub>3</sub>. *Angew Chem Int Ed* **49**, 2581-2584 (2010).

664 24 Schaub, T. & Paciello, R. A. A Process for the Synthesis of Formic Acid by CO<sub>2</sub>  
665 Hydrogenation: Thermodynamic Aspects and the Role of CO. *Angew Chem Int Ed* **50**,  
666 7278-7282 (2011).

667 25 Gunasekar, G. H., Shin, J., Jung, K.-D., Park, K. & Yoon, S. Design Strategy toward  
668 Recyclable and Highly Efficient Heterogeneous Catalysts for the Hydrogenation of CO<sub>2</sub> to  
669 Formate. *ACS Catal.* **8**, 4346-4353 (2018).

670 26 Feng, X. *et al.* Metal–Organic Frameworks Significantly Enhance Photocatalytic Hydrogen  
671 Evolution and CO<sub>2</sub> Reduction with Earth-Abundant Copper Photosensitizers. *J. Am. Chem.*  
672 *Soc.* **142**, 690-695 (2020).

673 27 Pullen, S., Fei, H., Orthaber, A., Cohen, S. M. & Ott, S. Enhanced Photochemical Hydrogen  
674 Production by a Molecular Diiron Catalyst Incorporated into a Metal–Organic Framework.  
675 *J. Am. Chem. Soc.* **135**, 16997-17003 (2013).

676 28 Saini, M. K., Korawat, H. S., Verma, S. K. & Basak, A. K. Pyridinium triflate catalyzed  
677 intramolecular alkyne-carbonyl metathesis reaction of O-propargylated 2-  
678 hydroxyarylaldehydes. *Tetrahedron Lett* **61**, 152657 (2020).

679 29 Guo, L. *et al.* Engineering heteroatoms with atomic precision in donor–acceptor covalent  
680 triazine frameworks to boost photocatalytic hydrogen production. *J. Mater. Chem. A* **6**,  
681 19775-19781 (2018).

682 30 Huang, W., He, Q., Hu, Y. & Li, Y. Molecular Heterostructures of Covalent Triazine  
683 Frameworks for Enhanced Photocatalytic Hydrogen Production. *Angew Chem Int Ed* **58**,  
684 8676-8680 (2019).

685 31 Ren, S. *et al.* Porous, Fluorescent, Covalent Triazine-Based Frameworks Via Room-  
686 Temperature and Microwave-Assisted Synthesis. *Adv Mater* **24**, 2357-2361 (2012).

687 32 Xu, R. *et al.* Rhenium-modified porous covalent triazine framework for highly efficient  
688 photocatalytic carbon dioxide reduction in a solid–gas system. *Catal. Sci. Technol.* **8**, 2224-  
689 2230 (2018).

690 33 Sun, D. *et al.* Construction of a supported Ru complex on bifunctional MOF-253 for  
691 photocatalytic CO<sub>2</sub> reduction under visible light. *Chem Commun* **51**, 2645-2648 (2015).

692 34 Wang, W. *et al.* Ru catalyst supported on bentonite for partial hydrogenation of benzene to  
693 cyclohexene. *Journal of Molecular Catalysis A: Chemical* **355**, 174-179 (2012).

694 35 Agnès, C. *et al.* XPS study of ruthenium tris-bipyridine electrografted from diazonium salt  
695 derivative on microcrystalline boron doped diamond. *Phys Chem Chem Phys* **11**, 11647-  
696 11654 (2009).

697 36 Karmakar, S., Barman, S., Rahimi, F. A. & Maji, T. K. Covalent grafting of molecular  
698 photosensitizer and catalyst on MOF-808: effect of pore confinement toward visible light-  
699 driven CO<sub>2</sub> reduction in water. *Energy Environ Sci* **14**, 2429-2440 (2021).

700 37 Peng, Z. *et al.* Hollow carbon shells enhanced by confined ruthenium as cost-efficient and  
701 superior catalysts for the alkaline hydrogen evolution reaction. *J. Mater. Chem. A* **7**, 6676-  
702 6685 (2019).

703 38 Li, J. *et al.* Van der Waals heterojunction for selective visible-light-driven photocatalytic  
704 CO<sub>2</sub> reduction. *Appl. Catal., B* **284**, 119733 (2021).

705 39 Xie, J. *et al.* Efficient visible light-driven water oxidation and proton reduction by an  
706 ordered covalent triazine-based framework. *Energy Environ Sci* **11** (2018).

707 40 Dresselhaus, M. S., Dresselhaus, G., Saito, R. & Jorio, A. Raman spectroscopy of carbon  
708 nanotubes. *Physics Reports* **409**, 47-99 (2005).

709 41 Shen, Y. *et al.* Defect-Abundant Covalent Triazine Frameworks as Sunlight-Driven Self-  
710 Cleaning Adsorbents for Volatile Aromatic Pollutants in Water. *Environ Sci Technol* **53**,  
711 9091-9101 (2019).

712 42 Kou, M. *et al.* Photocatalytic CO<sub>2</sub> conversion over single-atom MoN<sub>2</sub> sites of covalent  
713 organic framework. *Appl. Catal., B* **291**, 120146 (2021).

714 43 Zhang, H. *et al.* Isolated Cobalt Centers on W<sub>18</sub>O<sub>49</sub> Nanowires Perform as a Reaction  
715 Switch for Efficient CO<sub>2</sub> Photoreduction. *J. Am. Chem. Soc.* **143**, 2173-2177 (2021).

716 44 Wang, H. *et al.* Integrating Suitable Linkage of Covalent Organic Frameworks into  
717 Covalently Bridged Inorganic/Organic Hybrids toward Efficient Photocatalysis. *J. Am.*  
718 *Chem. Soc.* **142** (2020).

719 45 Guo, W., Cao, Z., Liu, Y. & Su, B. Electrochemiluminescence of a Vinyl-Functionalized  
720 Ruthenium Complex and Its Monolayer Formed through the Photoinduced Thiol-Ene Click  
721 Reaction. *ChemElectroChem* **4**, 1763-1767 (2017).

722 46 Gao, C., Wang, J., Xu, H. & Xiong, Y. Coordination chemistry in the design of  
723 heterogeneous photocatalysts. *Chem Soc Rev* **46**, 2799-2823 (2017).

724 47 Dong, L.-Z. *et al.* Stable Heterometallic Cluster-Based Organic Framework Catalysts for  
725 Artificial Photosynthesis. *Angew Chem Int Ed* **59**, 2659-2663 (2020).

726 48 Yang, C. *et al.* 2D/2D Ti<sub>3</sub>C<sub>2</sub> MXene/g-C<sub>3</sub>N<sub>4</sub> nanosheets heterojunction for high efficient  
727 CO<sub>2</sub> reduction photocatalyst: Dual effects of urea. *Appl. Catal., B* **268**, 118738 (2020).

728 49 Liu, J. *et al.* Solution Synthesis of Semiconducting Two-Dimensional Polymer via  
729 Trimerization of Carbonitrile. *J. Am. Chem. Soc.* **139**, 11666-11669 (2017).

730 50 Zhuo, T.-C. *et al.* H-Bond-Mediated Selectivity Control of Formate versus CO during CO<sub>2</sub>  
731 Photoreduction with Two Cooperative Cu/X Sites. *J. Am. Chem. Soc.* **143**, 6114-6122  
732 (2021).

733 51 Sampaio, R. N., Grills, D. C., Polyansky, D. E., Szalda, D. J. & Fujita, E. Unexpected Roles  
734 of Triethanolamine in the Photochemical Reduction of CO<sub>2</sub> to Formate by Ruthenium  
735 Complexes. *J. Am. Chem. Soc.* **142**, 2413-2428 (2020).

736 52 Machan, C. W., Sampson, M. D. & Kubiak, C. P. A Molecular Ruthenium Electrocatalyst  
737 for the Reduction of Carbon Dioxide to CO and Formate. *J. Am. Chem. Soc.* **137**, 8564-

738 8571 (2015).  
739 53 Wang, D., Huang, R., Liu, W., Sun, D. & Li, Z. Fe-Based MOFs for Photocatalytic CO<sub>2</sub>  
740 Reduction: Role of Coordination Unsaturated Sites and Dual Excitation Pathways. *ACS*  
741 *Catal.* **4**, 4254-4260 (2014).  
742 54 Zu, X. *et al.* Efficient and Robust Carbon Dioxide Electroreduction Enabled by Atomically  
743 Dispersed Sn<sup>δ+</sup> Sites. *Adv Mater* **31**, 1808135 (2019).  
744 55 Pang, H. *et al.* Cation Vacancy-Initiated CO<sub>2</sub> Photoreduction over ZnS for Efficient  
745 Formate Production. *ACS Energy Letters* **4**, 1387-1393 (2019).  
746 56 Li, Y., Li, B., Zhang, D., Cheng, L. & Xiang, Q. Crystalline Carbon Nitride Supported  
747 Copper Single Atoms for Photocatalytic CO<sub>2</sub> Reduction with Nearly 100% CO Selectivity.  
748 *ACS Nano* **14**, 10552-10561 (2020).  
749 57 Wang, J.-W. *et al.* Facile electron delivery from graphene template to ultrathin metal-  
750 organic layers for boosting CO<sub>2</sub> photoreduction. *Nature Communications* **12**, 813 (2021).  
751 58 Shan, B. *et al.* Binary molecular-semiconductor p–n junctions for photoelectrocatalytic  
752 CO<sub>2</sub> reduction. *Nature Energy* **4**, 290-299 (2019).  
753 59 Kuramochi, Y., Ishitani, O. & Ishida, H. Reaction mechanisms of catalytic photochemical  
754 CO<sub>2</sub> reduction using Re(I) and Ru(II) complexes. *Coord Chem Rev* **373**, 333-356 (2018).  
755 60 Anderson, P. A. *et al.* Designed Synthesis of Mononuclear Tris(heteroleptic) Ruthenium  
756 Complexes Containing Bidentate Polypyridyl Ligands. *Inorg Chem* **34**, 6145-6157 (1995).  
757 61 Chardon-Noblat, S., Deronzier, A., Ziessel, R. & Zsoldos, D. Selective Synthesis and  
758 Electrochemical Behavior of trans(Cl)- and cis(Cl)-[Ru(bpy)(CO)<sub>2</sub>Cl<sub>2</sub>] Complexes (bpy =  
759 2,2'-Bipyridine). Comparative Studies of Their Electrocatalytic Activity toward the  
760 Reduction of Carbon Dioxide. *Inorg Chem* **36**, 5384-5389 (1997).  
761 62 Huang, W. *et al.* Asymmetric Covalent Triazine Framework for Enhanced Visible-Light  
762 Photoredox Catalysis via Energy Transfer Cascade. *Angew Chem Int Ed* **57**, 8316-8320  
763 (2018).  
764 63 Bi, J. *et al.* A Cobalt-Modified Covalent Triazine-Based Framework as an Efficient  
765 Cocatalyst for Visible-Light-Driven Photocatalytic CO<sub>2</sub> Reduction. *ChemPlusChem* **84**,  
766 1149-1154 (2019).  
767

## 768 **Acknowledgements**

769 This work was supported by the National Natural Science Foundation of China (Nos. 51972345,  
770 51972342, and 22105226), Taishan Scholar Project of Shandong Province (No. ts20190922), Key  
771 Basic Research Project of Natural Science Foundation of Shandong Province (No. ZR2019ZD51),  
772 the Postdoctoral Research Foundation of China (2020M682253), Shandong Province Postdoctoral  
773 Innovative Talent Support Program (SDBX20200004).

## 774 **Author contributions**

775 Lu Wang designed the experiments, fabricated the materials and performed the photocatalytic

776 experiment. Lin Wang conceived the idea, designed the experiments. Saifei Yuan, Liping Song and  
777 Hao Ren completed the theoretical computations. Yuankang Xu, Manman He and Yuheng Zhang  
778 conducted the GC and XRD measurement. Jiangwei Zhang conducted the XANES and EXAFS  
779 analyses. Lu Wang wrote the manuscript. Lin Wang, Hang Wang, Yichao Huang, Tong Wei,  
780 Zhuangjun Fan and Yuichiro Himeda supervised the work and revised the manuscript. All authors  
781 contributed to discussion of the results and the manuscript preparation.

## 782 **Competing interests**

783 The authors declare no competing interests.

## Supplementary Files

This is a list of supplementary files associated with this preprint. Click to download.

- [SupportingInformationNC.pdf](#)